3-16-2011

Measurements of Branching Fractions for Electromagnetic Transitions Involving the χbJ(1P) States

Raymond Mountain
Syracuse University

Marina Artuso
Syracuse University

S. Blusk
Syracuse University

T. Skwarnicki
Syracuse University

CLNS 10/2071
CLEO 10-08

Measurements of branching fractions for electromagnetic transitions involving the $\chi_{bJ}(1P)$ states

M. Kornicer,[1] R. E. Mitchell,[1] C. M. Tarbert,[1] D. Besson,[2] T. K. Pedlar,[3] D. Cronin-Hennessy,[4] J. Hietala,[4] P. Zweber,[4] S. Dobbs,[5] Z. Metreveli,[5] K. K. Seth,[5] A. Tomaradze,[5] T. Xiao,[5] S. Brisbane,[6] L. Martin,[6] A. Powell,[6] P. Spradlin,[6] G. Wilkinson,[6] H. Mendez,[7] J. Y. Ge,[8] D. H. Miller,[8] I. P. J. Shipsey,[8] B. Xin,[8] G. S. Adams,[9] D. Hu,[9] B. Moziak,[9] J. Napolitano,[9] K. M. Ecklund,[10] J. Insler,[11] H. Muramatsu,[11] C. S. Park,[11] L. J. Pearson,[11] E. H. Thorndike,[11] F. Yang,[11] S. Ricciardi,[12] C. Thomas,[6,12] M. Artuso,[13] S. Blusk,[13] R. Mountain,[13] T. Skwarnicki,[13] S. Stone,[13] J. C. Wang,[13] L. M. Zhang,[13] G. Bonvicini,[14] D. Cinabro,[14] A. Lincoln,[14] M. J. Smith,[14] P. Zhou,[14] J. Zhu,[14] P. Naik,[15] J. Rademacker,[15] D. M. Asner,[16,*] K. W. Edwards,[16] K. Randrianarivony,[16] G. Tatishvili,[16,*] R. A. Briere,[17] H. Vogel,[17] P. U. E. Onyisi,[18] J. L. Rosner,[18] J. P. Alexander,[19] D. G. Cassel,[19] S. Das,[19] R. Ehrlich,[19] L. Fields,[19] L. Gibbons,[19] S. W. Gray,[19] D. L. Hartill,[19] B. K. Heltsley,[19] D. L. Kreinick,[19] V. E. Kuznetsov,[19] J. R. Patterson,[19] D. Peterson,[19] D. Riley,[19] A. Ryd,[19] A. J. Sadoff,[19] X. Shi,[19] W. M. Sun,[19] J. Yelton,[20] P. Rubin,[21] N. Lowrey,[22] S. Mehrabyan,[22] M. Selen,[22] J. Wiss,[22] and J. Libby[23]

(CLEO Collaboration)

[1] *Indiana University, Bloomington, Indiana 47405, USA*
[2] *University of Kansas, Lawrence, Kansas 66045, USA*
[3] *Luther College, Decorah, Iowa 52101, USA*
[4] *University of Minnesota, Minneapolis, Minnesota 55455, USA*
[5] *Northwestern University, Evanston, Illinois 60208, USA*
[6] *University of Oxford, Oxford OX1 3RH, UK*
[7] *University of Puerto Rico, Mayaguez, Puerto Rico 00681*
[8] *Purdue University, West Lafayette, Indiana 47907, USA*
[9] *Rensselaer Polytechnic Institute, Troy, New York 12180, USA*
[10] *Rice University, Houston, Texas 77005, USA*
[11] *University of Rochester, Rochester, New York 14627, USA*
[12] *STFC Rutherford Appleton Laboratory, Chilton, Didcot, Oxfordshire, OX11 0QX, UK*
[13] *Syracuse University, Syracuse, New York 13244, USA*
[14] *Wayne State University, Detroit, Michigan 48202, USA*
[15] *University of Bristol, Bristol BS8 1TL, UK*
[16] *Carleton University, Ottawa, Ontario, Canada K1S 5B6*
[17] *Carnegie Mellon University, Pittsburgh, Pennsylvania 15213, USA*
[18] *University of Chicago, Chicago, Illinois 60637, USA*
[19] *Cornell University, Ithaca, New York 14853, USA*
[20] *University of Florida, Gainesville, Florida 32611, USA*
[21] *George Mason University, Fairfax, Virginia 22030, USA*
[22] *University of Illinois, Urbana-Champaign, Illinois 61801, USA*
[23] *Indian Institute of Technology Madras, Chennai, Tamil Nadu 600036, India*

(Dated: December 2, 2010)

Abstract

Using $(9.32, 5.88)$ million $\Upsilon(2S, 3S)$ decays taken with the CLEO III detector, we obtain five product branching fractions for the exclusive processes $\Upsilon(2S) \to \gamma\chi_{b0,1,2}(1P) \to \gamma\gamma\Upsilon(1S)$ and $\Upsilon(3S) \to \gamma\chi_{b1,2}(1P) \to \gamma\gamma\Upsilon(1S)$. We observe the transition $\chi_{b0}(1P) \to \gamma\Upsilon(1S)$ for the first time. Using the known branching fractions for $\mathcal{B}[\Upsilon(2S) \to \gamma\chi_{bJ}(1P)]$, we extract values for $\mathcal{B}[\chi_{bJ}(1P) \to \gamma\Upsilon(1S)]$ for $J = 0$, 1, 2. In turn, these values can be used to unfold the $\Upsilon(3S)$ product branching fractions to obtain values for $\mathcal{B}[\Upsilon(3S) \to \gamma\chi_{b1,2}(1P)]$ for the first time individually. Comparison of these with each other and with the branching fraction $\mathcal{B}[\Upsilon(3S) \to \gamma\chi_{b0}]$ previously measured by CLEO provides tests of relativistic corrections to electric dipole matrix elements.

* Now at: Pacific Northwest National Laboratory, Richland, WA 99352

I. INTRODUCTION

The bottomonium ($b\bar{b}$) resonances display a rich pattern of electromagnetic transitions, including electric dipole (E1) transitions between S-wave ($\Upsilon(nS)$) and P-wave ($\chi_b(nP)$) states [1]. Branching fractions for these transitions involving the lowest $\chi_b(1P)$ states are summarized in Table I [2]. Notable in Table I is the suppression of the transitions from the $\Upsilon(3S)$ to the $\chi_{bJ}(1P)$ states. The electric dipole matrix element for the $\Upsilon(3S) \to \gamma\chi_{bJ}(1P)$ transition, $\langle 1P|r|3S\rangle$, is very small (see Ref. [3] for a discussion), and thus is quite sensitive to assumed shapes of wave functions due to various relativistic corrections. In the non-relativistic limit it should be independent of J, with the corresponding decay rates given by

$$\Gamma[\Upsilon(3S) \to \gamma\chi_{bJ}(1P)] = \frac{4}{3^5}\ \alpha\ (2J+1)\ E_\gamma^3\ |\langle 1P|r|3S\rangle|^2\ .$$

Thus, one would expect the rates for $J = 0 : 1 : 2$ to be governed by the term $E_\gamma^3 \times (2J+1)$, or to be in the ratio 1:2.4:3.6. Various treatments of relativistic corrections to these decay rates [4] imply ratios differing considerably from these values and from one another, providing an opportunity to distinguish between them.

TABLE I. Previous data [2] for branching fractions for electric dipole transitions in the bottomonium ($b\bar{b}$) system involving the lowest P-wave spin-triplet states $\chi_b(1P)$. Note the absence of measurements for $\Upsilon(3S) \to \gamma\chi_{b1,2}(1P)$ and $\chi_{b0}(1P) \to \gamma\Upsilon(1S)$.

Transition	E_γ (MeV)	$\mathcal{B}$ (%)
$\Upsilon(3S) \to \gamma\chi_{b0}(1P)$	483.9	0.30 ± 0.11
$\Upsilon(3S) \to \gamma\chi_{b1}(1P)$	452.1	< 0.17
$\Upsilon(3S) \to \gamma\chi_{b2}(1P)$	433.5	< 1.9
$\Upsilon(2S) \to \gamma\chi_{b0}(1P)$	162.5	3.8 ± 0.4
$\Upsilon(2S) \to \gamma\chi_{b1}(1P)$	129.6	6.9 ± 0.4
$\Upsilon(2S) \to \gamma\chi_{b2}(1P)$	110.4	7.15 ± 0.35
$\chi_{b0}(1P) \to \gamma\Upsilon(1S)$	391.1	< 6
$\chi_{b1}(1P) \to \gamma\Upsilon(1S)$	423.0	35 ± 8
$\chi_{b2}(1P) \to \gamma\Upsilon(1S)$	441.6	22 ± 4

As seen in Table I, the four photon energies for the cascade transitions $\Upsilon(3S) \to \gamma\chi_{b1,2}(1P) \to \gamma\gamma\Upsilon(1S)$ are all in the range 423–452 MeV in the rest frames of the decaying particle, making it difficult to extract the product branching fractions for individual values of J [5, 6]. Thus, until now, only the sum over J values (assumed here to be $J = 1, 2$) has been measured. For the summed product branching ratio,

$$\mathcal{B}_{\rm sum} = \sum_{J=1,2} \mathcal{B}[\Upsilon(3S) \to \gamma\chi_{bJ}(1P)] \times \mathcal{B}[\chi_{bJ}(1P) \to \gamma\Upsilon(1S)],$$

Ref. [5] obtains $\mathcal{B}_{\rm sum} = (1.2^{+0.4}_{-0.3} \pm 0.09) \times 10^{-3}$, while Ref. [6] obtains $\mathcal{B}_{\rm sum} = (2.14 \pm 0.22 \pm 0.21) \times 10^{-3}$.

In this article, we obtain separate product branching fractions for $J = 1$ and $J = 2$. Notice, however, that unfolding $\mathcal{B}[\Upsilon(3S) \to \gamma\chi_{b1,2}]$ from the product branching fractions requires knowledge of the $\chi_{b1,2}(1P) \to \gamma\Upsilon(1S)$ rates, which, as seen in Table I, have relative errors exceeding 20%. Therefore we also measure similar product branching fractions for $\Upsilon(2S)$ transitions, $\mathcal{B}[\Upsilon(2S) \to \gamma\chi_{bJ}(1P)] \times \mathcal{B}[\chi_{bJ}(1P) \to \gamma\Upsilon(1S)]$, from which the E1 rates for $\chi_{bJ}(1P)$ decays can be extracted by using the known $\Upsilon(2S)$ branching fractions in Table I. Thus, with product branching fractions for two-photon cascade transitions from $\Upsilon(3S)$ and $\Upsilon(2S)$ to $\Upsilon(1S)$ through $\chi_{bJ}(1P)$, we can make the first determinations of E1 branching fractions from $\Upsilon(3S)$ through $\chi_{bJ}(1P)$ for $J = 1$ and $J = 2$ and for $\chi_{b0}(1P)$ E1 transitions to $\Upsilon(1S)$, as well as improved values for $\chi_{b1,2}(1P) \to \gamma\Upsilon(1S)$. The branching fractions $\mathcal{B}[\Upsilon(3S) \to \gamma\chi_{b1,2}]$ may be compared with those for $J = 0$ previously measured by CLEO [7], $\mathcal{B}[\Upsilon(3S) \to \gamma\chi_{b0}(1P)] = (0.30 \pm 0.04 \pm 0.10)\%$, providing tests of relativistic corrections to electric dipole matrix elements such as those involved in the predictions of Refs. [4].

We discuss the data samples in Sec. II. We describe our analysis method in Sec. III, and our fits to the transitions $\Upsilon(2S) \to \gamma\chi_{bJ}(1P) \to \gamma\gamma\Upsilon(1S)$ and $\Upsilon(3S) \to \gamma\chi_{bJ}(1P) \to \gamma\gamma\Upsilon(1S)$ in Secs. IV and V, respectively. We summarize our results and compare theoretical predictions against the measured branching fractions $\mathcal{B}[\Upsilon(3S) \to \gamma\chi_{bJ}(1P)]$ in Sec. VI and against $\mathcal{B}[\chi_{bJ} \to \gamma\Upsilon(1S)]$ in Appendix A.

II. DATA SAMPLE

Our event selection criteria (and this entire analysis procedure) closely follow the analysis of $\Upsilon(2S) \to \eta\Upsilon(1S)$ [8]. The data used in this analysis were collected in e^+e^- collisions at the Cornell Electron Storage Ring (CESR), at center-of-mass energies at and ~ 25 MeV below the $\Upsilon(1S)$, $\Upsilon(2S)$, and $\Upsilon(3S)$ resonances. Integrated luminosities as well as the estimated numbers of these narrow resonance decays are shown in Table II. Events were recorded in the CLEO III detector, equipped with an electromagnetic calorimeter consisting of 7784 thallium-doped cesium iodide (CsI) crystals and covering 93% of solid angle, initially installed in the CLEO II [10] detector configuration. The energy resolution of the crystal calorimeter is 5% (2.2%) for 0.1 GeV (1 GeV) photons. The CLEO III tracking system [11] consists of a silicon strip detector and a large drift chamber, achieving a charged particle momentum resolution of 0.35% (1%) at 1 GeV/c (5 GeV/c) in a 1.5 T axial magnetic field.

TABLE II. Integrated luminosities of data sets used in this analysis, in units of pb^{-1}. "ON" corresponds to data sets taken in the vicinity of the nominal masses [2] of the corresponding narrow resonances, while "OFF" represents data taken ~ 25 MeV below the respective resonance masses. The estimated numbers of narrow resonance decays in each data set [9] are listed at the bottom row.

	$\Upsilon(1S)$	$\Upsilon(2S)$	$\Upsilon(3S)$
ON	1056	1305	1387
OFF	190	438	158
$\#\Upsilon(nS)$ (10^6)	20.81 ± 0.37	9.32 ± 0.14	5.88 ± 0.10

III. ANALYSIS METHOD

One can choose a set of $\ell^+\ell^-\gamma\gamma$ events ($\ell^\pm = e^\pm$ or $\mu^\pm$) in which the two photon energies sum up to a range consistent with the transition $\Upsilon(2S,3S) \to \gamma\chi_{bJ}(1P) \to \gamma\gamma\Upsilon(1S)$. We label the energy of the lower-energy photon $\mathrm{E}_\gamma^{\mathrm{low}}$, and that of the higher-energy photon $\mathrm{E}_\gamma^{\mathrm{high}}$. In this section, we describe how we select our lepton candidates from $\Upsilon(1S) \to \ell^+\ell^-$, how we apply kinematic constraints, and what our main backgrounds are.

A. Selection of leptons and photons

In order to identify leptonic decays of $\Upsilon(1S)$, we first select the two highest-momentum tracks in an event. We call a track an electron candidate if $E/p > 0.75$ or a muon candidate if $E/p < 0.20$, where E is the energy observed in the calorimeter shower associated with it and p is its momentum measured in the tracking system. Each track must satisfy $|\cos\theta| < 0.83$, where θ is the angle with respect to the positron beam direction, to ensure reliable triggering and optimal performances of the tracking system and calorimeter for lepton identification. These tracks must originate within 5 cm (5 mm) along the beam direction (in the r–ϕ plane) of the the interaction point (IP). Both tracks must be of the same lepton type and be of opposite charge.

Electron candidate tracks are dealt with somewhat differently, as they may radiate energy via bremsstrahlung, and also contain significant contamination from radiative Bhabha scattering. To recover bremsstrahlung, we add to each lepton candidate's four-momentum the four-momentum of any photon candidates found to lie within a cone of 100 mrad of the lepton candidate track direction at the IP. To suppress contributions from Bhabha scattering in $\gamma\gamma e^+e^-$ final states, we require e^+ candidates to satisfy $\cos\theta_{e^+} < 0.5$, where the final state positron makes an angle θ_{e^+} with the incoming positron beam direction. This selection criterion greatly suppresses Bhabha scattering background while keeping a large fraction of the signal.

Photon candidates must be detected either in the barrel ($|\cos\theta| < 0.81$) or in the endcaps ($0.85 < |\cos\theta| < 0.93$) of the calorimeter. Each must have a lateral shower profile consistent with that of a photon, and the shower energy must exceed 30 (50) MeV in the barrel (endcaps). Additionally, such showers must not be aligned with the initial momentum of a track.

B. Background composition

As in the analysis of $\Upsilon(2S,3S) \to \pi^0/\eta\Upsilon(1S,2S)$ [8], the dominant (and almost sole) sources of background are the doubly-radiative QED processes $e^+e^- \to \ell^+\ell^-\gamma\gamma$. Such events can completely satisfy the restrictions on kinematic fit quality (see below) when the $\ell^+\ell^-$ coincidentally has an invariant mass near that of the $\Upsilon(1S)$. Using our off-resonance data samples described in Table II to study these backgrounds, we find that such events produce smooth, nearly flat, nonpeaking spectra in $\mathrm{E}_\gamma^{\mathrm{low}}$ and $\mathrm{E}_\gamma^{\mathrm{high}}$. For the $\Upsilon(3S) \to \gamma\gamma\ell^+\ell^-$ analysis, we prepare Monte Carlo (MC) simulations of these processes for use in the nominal fits (see Sec. V A 2).

To improve photon resolutions, we use values of kinematically constrained four-vectors instead of the observed ones. We perform kinematic fitting on events in the following manner

(cf. Ref. [8]). We constrain the two leptons to have the $\Upsilon(1S)$ mass and the total four-momentum of the $\Upsilon(1S)$ candidate and the two photons to be that of the incoming e^+e^-, accounting for the non-zero crossing angle of the beams. The dilepton vertex is constrained to the beam spot, which itself is measured with multi-track hadronic events for each run of approximately 1 hour duration. The photons are assumed to originate at the beam spot.

The specific procedure employed is the following: Obtain reduced χ^2 values (i.e., values of χ^2 per degree of freedom) from the above vertex and momentum fits. Call them $\chi^2_{v,1C}$ and $\chi^2_{m,1C}$, respectively. Combine the mass-fitted object with two-photon candidates and constrain the sum of their four-momenta (a 4C fit) to the laboratory four-momentum, obtaining a reduced χ^2 value denoted by $\chi^2_{m,4C}$. Require reduced χ^2 values in the following order: (1) $\chi^2_{v,1C} < 10$; (2) $\chi^2_{m,1C} < 10$ (3) $\chi^2_{m,4C} < 5$.

Our kinematic fitting software assumes that measured distributions are Gaussian, but there are well-understood and reasonably well-modeled low-side tails on the energy response of the calorimeter. Hence, the (reduced) χ^2 distributions from fits in both MC and data will also have tails not seen in formal χ^2 probability distributions. Good agreement of the reduced χ^2 distributions between data and MC is essential. We explored this agreement in previous CLEO analyses [12] and in this analysis (Sec. IV C 4). We included the small discrepancies we found in our systematic errors.

Figure 1 shows distributions of one of our reduced χ^2 variables, $\chi^2_{m,4C}$, for the $\Upsilon(2S,3S) \to \gamma\gamma\Upsilon(1S)$ analyses. Standard and alternate restrictions on these variables are indicated in the figure. The overlaid histograms indicate the contributions of MC signal and background, weighted by our final measured values. Based on the scaled off-resonance data, the expected background levels in the signal regions correspond to background-to-signal ratios of $\sim$ 1.5 (3)% for the $\Upsilon(1S) \to \mu^+\mu^-$ candidates and $\sim$ 15 (20)% for the $\Upsilon(1S) \to e^+e^-$ candidates in $\Upsilon(2S)$ ($\Upsilon(3S)$) decays.

IV. ANALYSIS OF $\Upsilon(2S) \to \gamma\gamma\ell^+\ell^-$ VIA $\chi_{bJ}(1P)$

Because the expected $E_\gamma^{\rm low}$ spectra (110–160 MeV) have excellent separation of decays through different $\chi_{bJ}(1P)$ spin states, we can obtain the yields of the individual J contributions with a fit to $E_\gamma^{\rm low}$, without regard to $E_\gamma^{\rm high}$ (390–440 MeV). The $E_\gamma^{\rm low}$ spectra exhibit three clearly distinguishable peaks with known peak energies and resolutions entirely dominated by measurement effects, although detector resolution is improved upon by the constrained fit. Figure 2 illustrates the $E_\gamma^{\rm low}$ distributions from data, along with the fits described in the following subsections.

A. Signal Monte Carlo samples

We use the EVTGEN event generator [13] to generate expected signal shapes in Monte Carlo (MC) simulations. To simulate the photon angular distributions, we assume that the radiative transitions are pure electric dipole. We generate 100 k events with $\mathcal{B}[\Upsilon(2S) \to \gamma\chi_{bJ}(1P)] = \mathcal{B}[\chi_{bJ} \to \gamma\Upsilon(1S)] = 100\%$ while $\mathcal{B}[\Upsilon(1S) \to e^+e^-] = \mathcal{B}[\Upsilon(1S) \to \mu^+\mu^-] = 50\%$ for each of $J = 0$, 1, and 2. We fit each of the MC distributions of $E_\gamma^{\rm low}$ with a double Gaussian whose difference between the two means we allow to float. Resultant reconstruction efficiencies are shown in Table III.

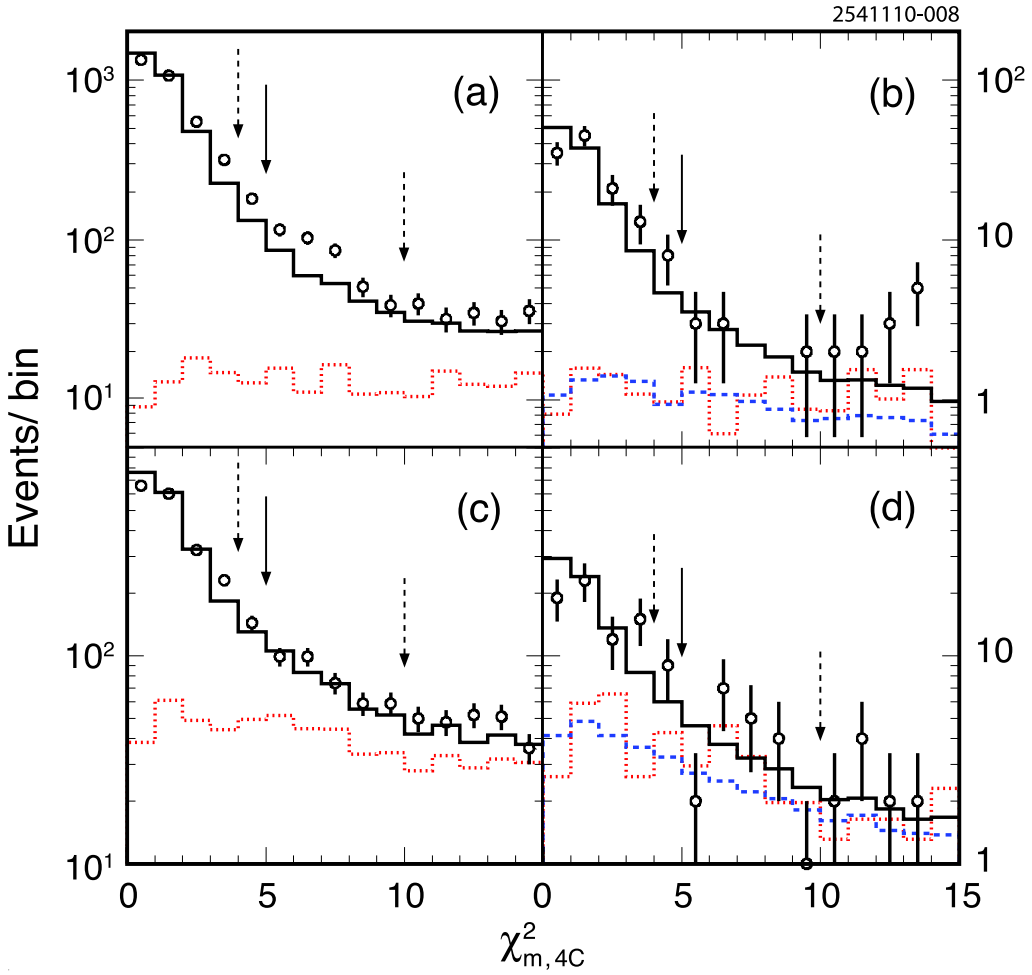

FIG. 1. Distributions of $\chi^2_{m,4C}$ for $\Upsilon(1S) \to \mu^+\mu^-$ candidates (a,b) and $\Upsilon(1S) \to e^+e^-$ candidates (c,d) based on events of $\Upsilon(2S) \to \gamma\gamma\Upsilon(1S)$ candidates (a,c) and $\Upsilon(3S) \to \gamma\gamma\Upsilon(1S)$ candidates (b,d) via $\chi_{bJ}(1P)$, respectively. Open circles represent data, solid histograms the sum of scaled signal MC and background contributions, where the background levels are indicated by scaled off-resonance data (dotted histogram) and, for $\Upsilon(3S)$ decays, QED MC simulation (dashed histograms). Solid arrows indicate standard selection criteria, and dashed arrows alternate values used for systematic studies of dependence on selection criteria.

B. Fitting the data

Our nominal fit procedure is to take these double Gaussian shapes based on the signal MC samples to fit to data, fixing the respective narrower Gaussian widths and differences between the two Gaussian means but allowing the larger widths (σ_J where $J = 0$, 1, and 2) to float. We use a flat background shape whose normalization is also allowed to float. We then perform a maximum likelihood fit. Figure 2 shows fits to data for $\Upsilon(1S) \to \mu^+\mu^-$ candidates (a,b) and $\Upsilon(1S) \to e^+e^-$ candidates (c,d) with flat background shapes represented by the dashed histograms, while the dotted histograms are based on scaled off-$\Upsilon(2S)$-resonance data. In Fig. 2(b), we zoom in to a smaller vertical scale to emphasize the $J = 0$ component, which is clearly visible for the $\mu^+\mu^-$ candidates. However, in Fig. 2(d) the $J = 0$ peak is

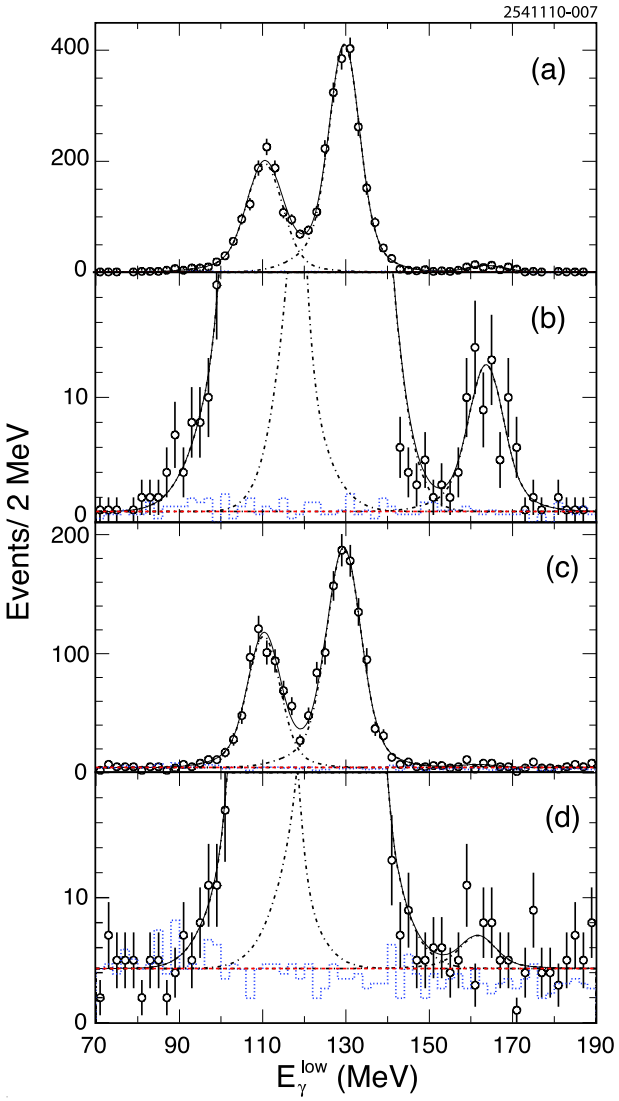

FIG. 2. Fits to data with a flat background shape represented by dashed histograms for $\Upsilon(1S) \to \mu^+\mu^-$ $[e^+e^-]$ candidates in the two plots (a,b) [(c,d)]. Plots (b) and (d) are identical, respectively, to (a) and (c) but zoomed in so as to highlight the $J = 0$ component. The dotted histograms represent the scaled background shapes based on the off-resonance data. The dot-dashed lines show components of each of the three photon lines.

obscured by the relatively larger background in the e^+e^- candidates. To compensate for the larger backgrounds in the distributions for the the e^+e^- candidates, we fix the ratio of the widths of the $J = 0$ peak to the width of the $J = 1$ peak (σ_0/σ_1) to be equal to the ratio obtained for the signal MC samples. (In our systematic study, we remove this restriction and observe the deviation from our central value.) The observed yields, along with efficiency-corrected products of branching fractions, are shown in Table III. The last column of Table III (labeled as "All J") represents measurements of these same two photon cascade events, but is summed over J for $J = 0$, 1, and 2. We obtain the yield simply by subtracting the fitted background shape, with normalization determined from the nominal fit, and then by summing the resultant spectrum over the signal region. There, efficiencies

TABLE III. Fitted yields, reconstruction efficiencies (ϵ), and corresponding branching fractions are shown with statistical errors only. Here, $\mathcal{B}1 = \mathcal{B}[\Upsilon(2S) \to \gamma\chi_{bJ}(1P)]$, $\mathcal{B}2 = \mathcal{B}[\chi_{bJ}(1P) \to \gamma\Upsilon(1S)]$, and $\mathcal{B}3 = \mathcal{B}[\Upsilon(1S) \to \ell^+\ell^-]$. The last column ("All J") shows results for the sum of $J = 0$, 1, and 2 components obtained by subtracting fits to the backgrounds from the data, as described in the text.

	$\ell^+\ell^-$	$J = 0$	$J = 1$	$J = 2$	All J
Yields	e^+e^-	16 ± 9	1068 ± 36	600 ± 30	1684 ± 41
Yields	$\mu^+\mu^-$	71 ± 10	2154 ± 50	1170 ± 39	3395 ± 58
ϵ (10^{-2})	e^+e^-	20.9 ± 0.2	21.3 ± 0.2	20.2 ± 0.2	20.9 ± 0.2
ϵ (10^{-2})	$\mu^+\mu^-$	38.6 ± 0.3	39.9 ± 0.3	37.7 ± 0.3	39.1 ± 0.2
$\mathcal{B}1 \times \mathcal{B}2 \times \mathcal{B}3$ (10^{-4})	e^+e^-	0.083 ± 0.044	5.38 ± 0.18	3.19 ± 0.16	8.66 ± 0.21
$\mathcal{B}1 \times \mathcal{B}2 \times \mathcal{B}3$ (10^{-4})	$\mu^+\mu^-$	0.196 ± 0.028	5.79 ± 0.13	3.33 ± 0.11	9.32 ± 0.16
$\mathcal{B}1 \times \mathcal{B}2 \times \mathcal{B}3$ (10^{-4})	e^+e^- and $\mu^+\mu^-$	0.163 ± 0.024	5.65 ± 0.11	3.29 ± 0.09	9.08 ± 0.13

are weighted by the measured branching fractions for each spin state. The χ^2 values for the fits are 50.1 for 60 data points (minus 9 parameters), c.l. = 51.0% for $\Upsilon(1S) \to e^+e^-$, and 51.4 for 60 data points (minus 10 parameters), c.l. = 42.0% for $\Upsilon(1S) \to \mu^+\mu^-$.

C. Systematic uncertainties

Systematic uncertainties are assessed as J-independent contributions that impact the yields of several modes equally, or are determined individually. Where errors differ for e^+e^- and $\mu^+\mu^-$ candidates, they are averaged with the same statistical weights used for combining the respective product branching fractions.

1. *Uncertainties common to both e^+e^- and $\mu^+\mu^-$ candidates*

The uncertainties common to both e^+e^- and $\mu^+\mu^-$ candidates are relative uncertainties known already from external sources, and which impact every yield identically. The relative uncertainties on the numbers of resonance decays in our data sets were estimated in Ref. [9]. We take the dilepton reconstruction systematic uncertainty from Ref. [14] as 1.0%, since our dilepton reconstruction is identical to that used there. Similarly we use the result from that paper for π^0-finding, which was 1.6% per π^0. We therefore use this as an estimate of the uncertainty for reconstructing the two photons in the cascade, since the photon energies we are studying in this analysis very closely resemble the photon energies in Ref. [14], and otherwise the processes are kinematically very similar. Instead of 1.6% for the pair, we round up to 2.0% to be conservative.

2. Signal shapes

In our nominal fit procedure, we take a double Gaussian, fitted to the signal MC samples, to represent the signal line shapes but float the larger widths of the Gaussians for the fits to data to accommodate imperfect simulations of detector resolutions. Here, we have tried the following variations:

- Constrain all σ_J in both $\Upsilon(1S) \to \ell^+\ell^-$ candidates while requiring the ratios σ_0/σ_1 and σ_2/σ_1 to be the same as in our signal MC samples.
- Do not constrain the "σ" in either lepton flavor.

3. Background shape

The only backgrounds predicted by a MC simulation of all $\Upsilon(2S)$ decays are from $\Upsilon(2S) \to \pi^0\pi^0\Upsilon(1S)$. Even so, this background source is found to be negligible because it contributes only 5-10 events to the signal regions and it has no significant structure in photon energy. Hence, to the extent it matters at all, it will tend to get absorbed into the background shape in the fit. Backgrounds from $\Upsilon(2S) \to \pi^0/\eta\Upsilon(1S)$, using the recently measured branching fractions [8], are also found to be insignificant.

To represent our background, whose main compositions are either doubly-radiative Bhabha events or μ-pairs, we use a flat shape with floating normalization in our nominal fit. To probe the sensitivity to the fitted yields due to this assumption, we try a first-order polynomial.

To determine possible systematical effects due to the fixed background normalization in the "All J" procedure, we vary the background by ± 1 σ of the statistical uncertainty observed in our nominal procedure.

4. Kinematic fit reduced χ^2 requirements

We consider different choices in reduced χ^2 criteria for our vertex and four-momentum fits. The four variations to our standard selection are: $\chi^2_{m,4C} < 4$ or < 10 rather than 5, $\chi^2_{m,1C} < 5$ rather than 10, and $\chi^2_{v,1C} < 5$ rather than 10. The spin of the $\chi_{bJ}(1P)$ state should have almost no influence on how these reduced χ^2 distributions are simulated, so to increase statistical stability on the resultant variations, we take variations from the "All J" procedure to assign this systematic uncertainty.

5. Lepton flavor difference

We have also assessed possible systematic uncertainties due to the difference between e^+e^- and $\mu^+\mu^-$ results by calculating the yield for the sum of $J = 1$ and $J = 2$ for e^+e^- and then for $\mu^+\mu^-$. (As in the case of determining possible uncertainties due to requirements on the fitted reduced χ^2, the spin of the $\chi_{bJ}(1P)$ state should have no influence on whether leptons are correctly reconstructed.) We then took half the difference between the yields obtained for each lepton flavor, and divided by the average yield as an estimate of the relative systematic uncertainty arising from lepton flavor differences.

6. Additional contributing uncertainties

Other possible systematical effects we have investigated include: variations in fit ranges, histogram binning, statistical uncertainties in signal MC samples, uncertainties in the measured $\mathcal{B}[\Upsilon(2S) \to \gamma\chi_{bJ}(1P)] \times \mathcal{B}[\chi_{bJ}(1P) \to \gamma\Upsilon(1S)]$ to weight efficiencies for the "All J" case, as well as cuts on E/p to identify lepton species.

Table IV shows sources of systematic uncertainties we have considered for this analysis.

TABLE IV. Fractional uncertainties (in %) on the combined-dilepton product branching fractions, $\mathcal{B}[\Upsilon(2S) \to \gamma\chi_{bJ}(1P)] \times \mathcal{B}[\chi_{bJ}(1P) \to \gamma\Upsilon(1S)] \times \mathcal{B}[\Upsilon(1S) \to \ell^+\ell^-]$, due to variations of the listed selection criteria and fit procedures. The last column ("All J") shows fit results for the sum of the three two-photon cascades via $\chi_{bJ}(1P)$ states for $J = 0$, 1, and 2. For this last column, the entry for "MC simulation" includes not only statistical errors on reconstruction efficiencies, but also the effect of total uncertainties of the measured branching fractions on the weighted efficiency.

Contribution	$J=0$	$J=1$	$J=2$	All J
$N_{\Upsilon(2S)}$		1.5		
Track-finding		1.0		
Photon-finding		2.0		
Reduced χ^2 requirement		1.4		
Lepton identification		0.4		
Lepton flavor difference		3.6		
Fit range	7.1	0.2	0.7	0.4
Signal shape	1.4	0.5	0.6	—
QED bkg shape	1.9	0.01	0.2	0.9
Bin width	1.6	0.04	0.01	0.01
MC simulation	0.8	0.8	0.8	0.6
Total	9.0	4.8	4.9	4.9

D. Results on analysis of $\Upsilon(2S) \to \gamma\gamma\ell^+\ell^-$

Table V shows our final results for our $\Upsilon(2S)$ analysis as well as those from other experiments.

V. ANALYSIS OF $\Upsilon(3S) \to \gamma\gamma\ell^+\ell^-$ VIA $\chi_{bJ}(1P)$

In the case of the three transitions $\Upsilon(3S) \to \gamma\chi_{bJ}(1P) \to \gamma\gamma\Upsilon(1S)$, the higher and lower energy photons have similar energies. Furthermore, among these transitions in some cases the higher energy photon is emitted from the $\Upsilon(3S)$, and in some cases the higher energy photon is emitted from the boosted $\chi_{bJ}(1P)$. Therefore, instead of fitting just one distribution, as we do for the $\Upsilon(2S)$ analysis, we maximize our use of information and fit the two-dimensional histogram of E_γ^{low} vs. E_γ^{high}, where $E_\gamma^{low} < E_\gamma^{high}$ are kinematically constrained E_γ. Our fit

TABLE V. Final results of this analysis. Here, $\mathcal{B}1 = \mathcal{B}[\Upsilon(2S) \to \gamma\chi_{bJ}(1P)]$, $\mathcal{B}2 = \mathcal{B}[\chi_{bJ}(1P) \to \gamma\Upsilon(1S)]$, and $\mathcal{B}3 = \mathcal{B}[\Upsilon(1S) \to \ell^+\ell^-]$. We use $\mathcal{B}3 = (2.48 \pm 0.05)\%$ [2] and $\mathcal{B}1$ values from Table I to extract $\mathcal{B}1 \times \mathcal{B}2$ as well as $\mathcal{B}2$. The last column ("All J") shows fit results for the sum over $J = 0$, 1, and 2. Again, the first errors are statistical, the second errors are systematic, and the third errors (when applicable) are uncertainties due to uncertainties in $\mathcal{B}1$ and/or $\mathcal{B}3$. In the bottom half of the table we also show results from other experiments for a comparison.

	$J=0$	$J=1$	$J=2$	All J
$\mathcal{B}1 \times \mathcal{B}2 \times \mathcal{B}3$ (10^{-4})	$0.163 \pm 0.024 \pm 0.015$	$5.65 \pm 0.11 \pm 0.27$	$3.29 \pm 0.09 \pm 0.16$	$9.08 \pm 0.13 \pm 0.44$
$\mathcal{B}1 \times \mathcal{B}2$ (10^{-3})	$0.659 \pm 0.096 \pm 0.059 \pm 0.013$	$22.8 \pm 0.4 \pm 1.1 \pm 0.5$	$13.3 \pm 0.4 \pm 0.6 \pm 0.3$	$36.7 \pm 0.6 \pm 1.8 \pm 0.7$
$\mathcal{B}2$ (10^{-2})	$1.73 \pm 0.25 \pm 0.16 \pm 0.19$	$33.0 \pm 0.6 \pm 1.6 \pm 2.0$	$18.5 \pm 0.5 \pm 0.9 \pm 1.0$	—
Values of $\mathcal{B}2$ (10^{-2}) from other experiments				
PDG average [2]	< 6 at 90% CL	35 ± 8	22 ± 4	—
Crystal Ball [15]	< 6 at 90% CL	$32 \pm 6 \pm 7$	$27 \pm 6 \pm 6$	—
CUSB	< 11 at 90% CL [16]	47 ± 18 [17]	20 ± 5 [17]	—

will utilize the 2D histograms from our signal Monte Carlo for each of the $J = 0, 1$, and 2 samples, as well as MC samples of doubly-radiative Bhabha events and μ-pairs.

A. Monte Carlo samples

1. *Signal MC for* $\Upsilon(3S) \to \gamma\chi_{bJ}(1P)$

Approximately 100k events for each spin were generated for each of the $\chi_{bJ}(1P)$ subsamples, where $\Upsilon(3S) \to \gamma\chi_{bJ}(1P)$ at 100%, $\chi_{bJ}(1P) \to \gamma\Upsilon(1S)$ at 100% and with $\Upsilon(1S)$ decaying half the time to each of $\mu^+\mu^-$ and e^+e^-. These samples were used to generate the three relevant 2D histograms of $E_\gamma^{\rm low}$ vs. $E_\gamma^{\rm high}$ for each spins. In projections of these histograms on the $E_\gamma^{\rm high}$ and $E_\gamma^{\rm low}$ axes, for $J = 0$ and $J = 1$, the higher-energy photon has a sharp distribution, while the lower-energy photon is Doppler-broadened (see Table I). For $J = 2$, the situation is reversed to a large extent.

Figure 3 shows the $E_\gamma^{\rm low}$ vs. $E_\gamma^{\rm high}$ two-dimensional histogram for $\Upsilon(3S)$ signal MC samples, weighted according to our final measured branching fractions. Notice that the events are restricted to the diagonal band by two simple kinematic facts: first, that $E_\gamma^{\rm low} < E_\gamma^{\rm high}$, and second, that the invariant mass recoiling against the two photons has been constrained to that of the $\Upsilon(1S)$. The lower boundary line corresponds to the case in which the photon three-momenta have zero opening angle in the initial e^+e^- rest frame (recoiling against the dilepton pair with maximum possible combined momentum), and the upper boundary line to the case in which the photon momenta directly oppose one another (with the softer one traveling along the same direction as the $\Upsilon(1S)$ candidate, and the more energetic one in the opposite direction). Note that the boundaries are purely kinematic in nature due to the $\Upsilon(1S)$ mass constraint, and hold for background as well as signal events. In Fig 3, these limits are labeled $\Theta_{\gamma\gamma} = 0$ and π, respectively.

The population within the band is directly related to the cosine of the angle $\theta_{\gamma\gamma}$ between the two photons in the rest frame of the $\chi_{bJ}(1P)$. The distributions $W_J(\cos\theta_{\gamma\gamma})$ for $J = 1, 2$,

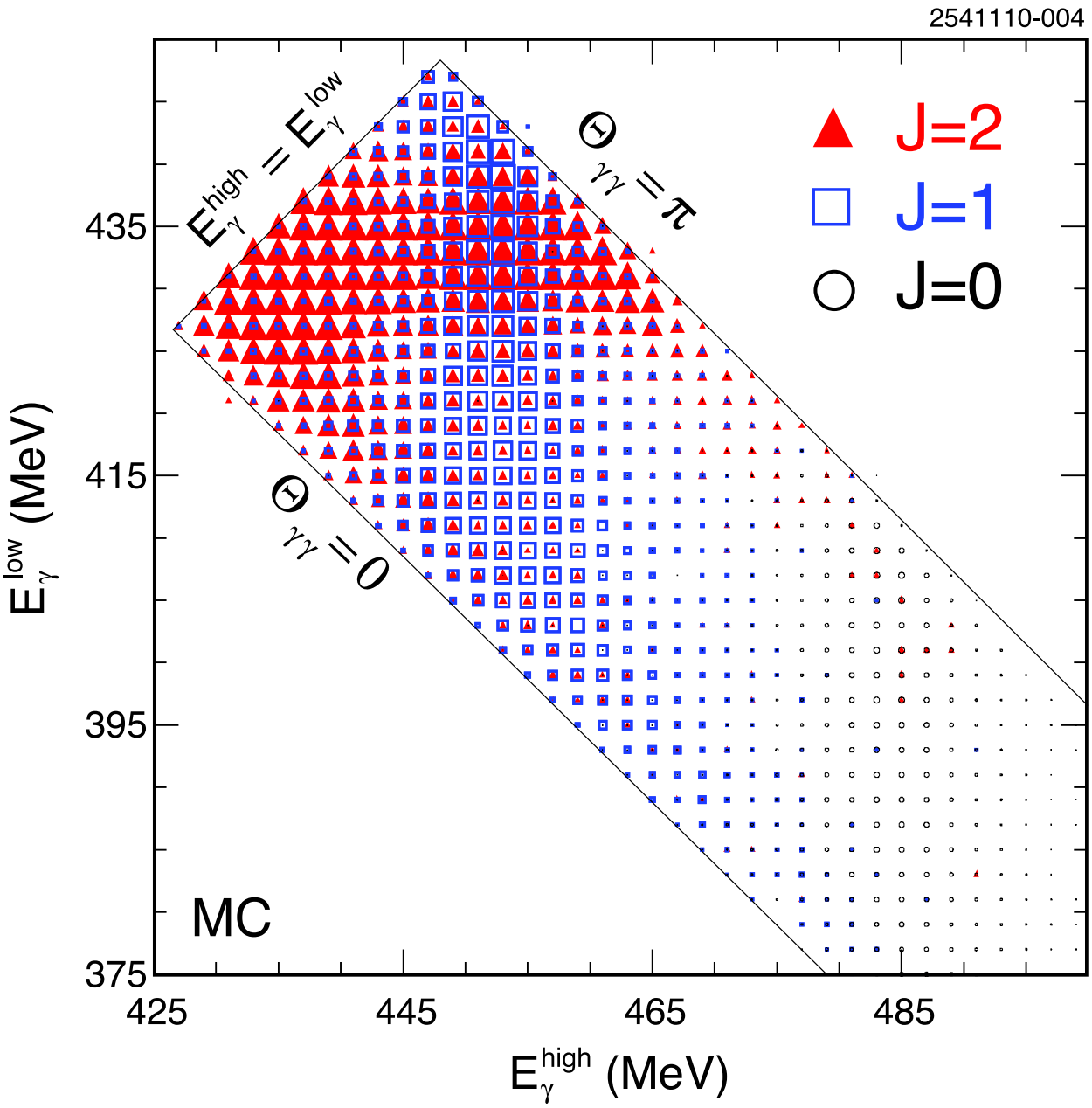

FIG. 3. Distributions of E_γ^{low} vs. E_γ^{high} based on $\Upsilon(3S)$ signal MC samples for $J = 0$ (open circles), $J = 1$ (open rectangles), and $J = 2$ (closed triangles) using $\mu^+\mu^-$ selection. The diagonal band, edged by lines labeled as $\Theta_{\gamma\gamma} = \pi$ (or 0), where $\Theta_{\gamma\gamma}$ is an opening angle between the two emitted photons, is generated due to our kinematic constraints. The three samples are normalized to our measured production rates in this work while the size of a symbol in a bin is proportional to the number of events for the corresponding J in that bin.

normalized so that their integral over $\cos\theta_{\gamma\gamma}$ is 1, are

$$W_1(\cos\theta_{\gamma\gamma}) = \frac{15}{32}(1+\frac{1}{5}\cos^2\theta_{\gamma\gamma}) \ , \tag{1}$$

$$W_2(\cos\theta_{\gamma\gamma}) = \frac{1}{160}(73+21\cos^2\theta_{\gamma\gamma}) \ , \tag{2}$$

implying a slight enhancement at each end of the $\cos\theta_{\gamma\gamma}$ range and hence at maximum and minimum Doppler-broadened photon energy. This feature is present in all of our signal MC samples that take account of the photon angular distributions properly. The respective reconstruction efficiencies are shown in Table VI.

TABLE VI. Fitted yields, reconstruction efficiencies (ϵ), and corresponding branching fractions are shown. Here, $\mathcal{B}1 = \mathcal{B}[\Upsilon(3S) \to \gamma\chi_{bJ}(1P)]$, $\mathcal{B}2 = \mathcal{B}[\chi_{bJ}(1P) \to \gamma\Upsilon(1S)]$, and $\mathcal{B}3 = \mathcal{B}[\Upsilon(1S) \to \ell^+\ell^-]$. The last column ("$J = 1$ and 2") shows results of sum of the two two-photon cascades via $\chi_{bJ}(1P)$ states for 1 and 2 obtained by subtracting fits to the backgrounds from the data, as described in the text.

	$\ell^+\ell^-$	$J=1$	$J=2$	$J=1$ and 2
Yields	e^+e^-	12 ± 6	48 ± 9	61 ± 8
Yields	$\mu^+\mu^-$	38 ± 9	78 ± 11	117 ± 11
ϵ (10^{-2})	e^+e^-	22.3 ± 0.2	21.3 ± 0.2	21.6 ± 0.2
ϵ (10^{-2})	$\mu^+\mu^-$	41.1 ± 0.2	38.8 ± 0.2	39.5 ± 0.2
$\mathcal{B}1 \times \mathcal{B}2 \times \mathcal{B}3$ (10^{-5})	e^+e^-	0.91 ± 0.49	3.88 ± 0.70	4.79 ± 0.61
$\mathcal{B}1 \times \mathcal{B}2 \times \mathcal{B}3$ (10^{-5})	$\mu^+\mu^-$	1.58 ± 0.38	3.40 ± 0.49	5.06 ± 0.47
$\mathcal{B}1 \times \mathcal{B}2 \times \mathcal{B}3$ (10^{-5})	e^+e^- and $\mu^+\mu^-$	1.33 ± 0.30	3.56 ± 0.40	4.96 ± 0.37

2. Background from QED processes

Only the processes $e^+e^- \to \gamma\gamma(e^+e^-, \mu^+\mu^-)$ (and to a much lesser extent, $\Upsilon(3S) \to \pi^0\pi^0\Upsilon(1S)$) can be reasonably expected to contribute much background. To represent the doubly-radiative QED events, we prepare MC samples generated via the Babayaga event generator [18] with sizes of roughly 100 (200) times larger luminosity than what the data have for doubly-radiative Bhabha (μ-pair) events, respectively. The very large number of QED events are then reduced with a very loose selection at the generator level to have at least two photons and a dilepton invariant mass near that of the $\Upsilon(1S)$. Only those chosen events are passed along to the next stage of processing, the CLEO detector simulation.

B. Fitting the data

Figure 4 shows a distribution of $E_\gamma^{\rm low}$ vs. $E_\gamma^{\rm high}$ based on the on-$\Upsilon(3S)$ data. To constrain the backgrounds in our fits, we use fit ranges for $E_\gamma^{\rm low}$ and $E_\gamma^{\rm high}$ larger than the ranges illustrated in the figure. We choose our fit ranges to be ($420 < E_\gamma^{\rm high} < 560$) MeV and

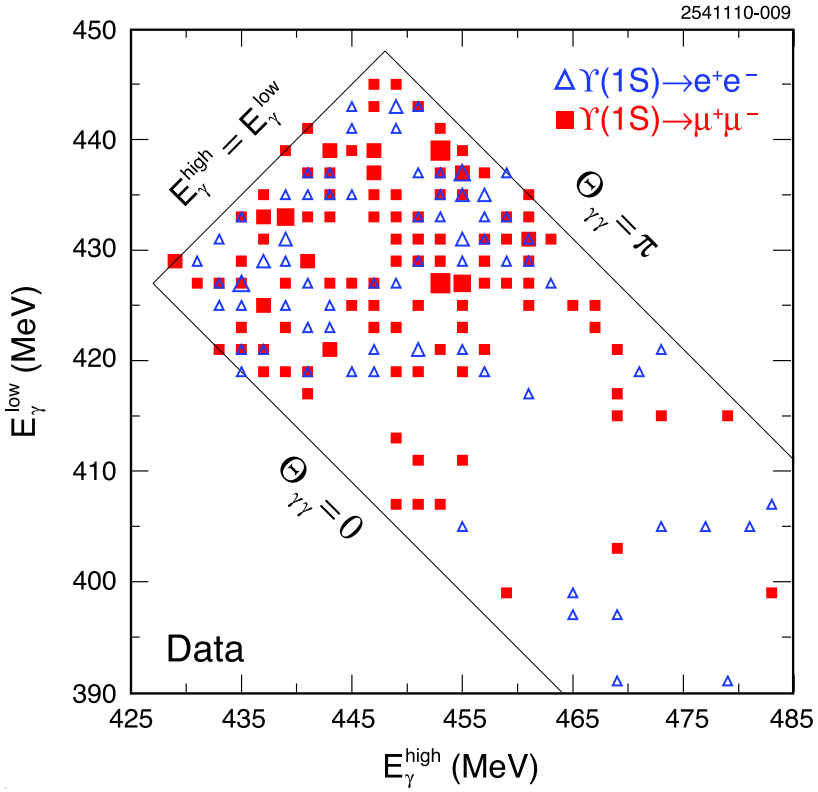

FIG. 4. Distributions of E_γ^{low} vs. E_γ^{high} based on the on-$\Upsilon(3S)$ data. Open triangles (closed rectangles) represent data points based on e^+e^- ($\mu^+\mu^-$) selection. The size of each symbol is proportional to the number of events in the bin.

($340 < E_\gamma^{low} < 460$) MeV. While the upper (lower) bound of E_γ^{low}(E_γ^{high}) does not matter much because of bins containing no events, the choice of the lower (upper) bound of E_γ^{low}(E_γ^{high}) controls the statistics available for fitting the backgrounds. Since the minimum E_γ^{low} is related to the maximum E_γ^{high} by the kinematic constraints, we study the variation of the background scale factor as a function of the maximum E_γ^{high}. Based on this exercise, we choose the maximum E_γ^{high} to be 560 MeV and the minimum $E_\gamma^{low} = 340 (\simeq 900 - 560)$ MeV where $E_\gamma^{high} + E_\gamma^{low} \simeq 900$ values for which the fitted normalization scale factors become stable compared to the sizes of their statistical errors.

Using the QED MC background histograms as the background function and the three signal Monte Carlo samples, and fixing the normalization of the $J = 0$ component with the measured $\mathcal{B}[\Upsilon(3S) \to \gamma\chi_{b0}(1P)]$ [9] and $\mathcal{B}[\chi_{b0}(1P) \to \gamma\Upsilon(1S)]$ (this work), we perform a maximum likelihood fit to the the 2D data distribution in E_γ^{low} vs. E_γ^{high}. We float the normalizations of both background and signals (for $J = 1$ and 2 only). The results of the fits projected onto the two photon-energy axes are shown in Fig. 5.

We also extract signal yield by subtracting the fitted background shape, with normalization fixed based on the above nominal fit procedure, and then by summing the resultant distribution over the signal region. This yield corresponds to the one from *both* transitions, $\Upsilon(3S) \to \gamma\gamma\ell^+\ell^-$ via $\chi_{bJ}(1P)$ for $J = 1$ and 2. The observed yields, along with efficiency-corrected branching fractions, are shown in Table VI.

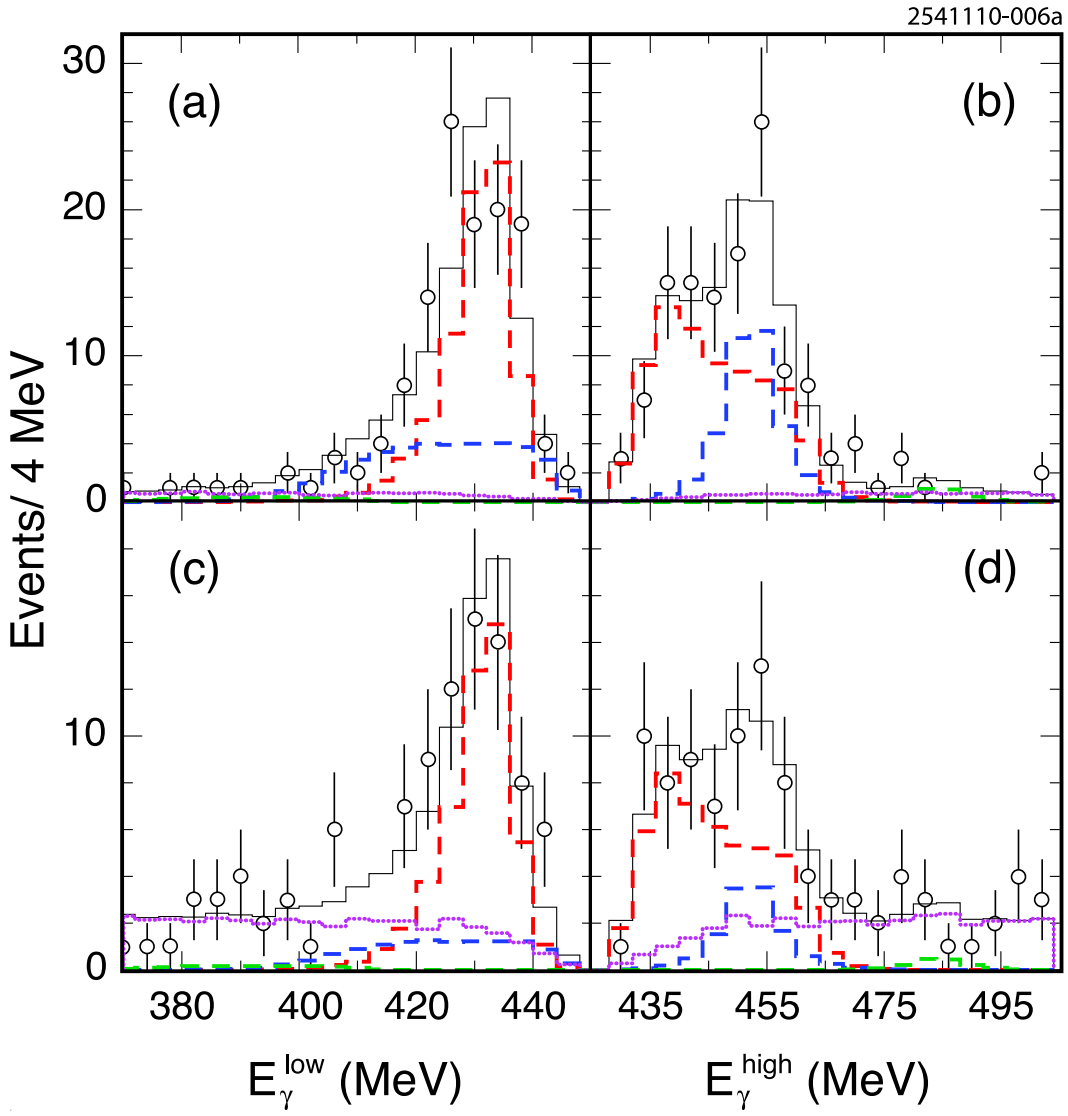

FIG. 5. Projections from the nominal fit to data onto (a,c) E_γ^{low} and (b,d) E_γ^{high} axes for data using the (a,b) $\mu^+\mu^-$ and (c,d) e^+e^- selections. The dashed histograms represent signal photons via $\chi_{bJ}(1P)$. The dotted histograms represent the QED MC sample contribution as normalized by the fit, and the solid histogram is the sum of background and signal histograms.

C. Systematic uncertainties

We study the systematic uncertainties in a similar way as in Sec. IV C. We mention only studies whose methods differ from the description given in Sec. IV C. Table VII shows a summary of estimated systematic uncertainties.

1. Binning scheme

We calculate the branching fractions using 4 MeV bins instead of the nominal 2 MeV bins. Besides a difference in bin sizes, we also consider a difference in bin shapes with a

distribution of $E_{\rm SUM}$ $(= {\rm E}_\gamma^{\rm low} + {\rm E}_\gamma^{\rm high})$ vs. $E_{\rm DIFF}$ $(= {\rm E}_\gamma^{\rm high} - {\rm E}_\gamma^{\rm low})$.

2. Photon energy resolution

In order to account for the possibility that the width of the signal MC photon distributions may not accurately reflect the width of the photon distributions in data, we have generated additional signal MC sets with the detector resolution broadened and narrowed by 10% of itself and recalculated the branching fractions using these altered MC sets.

3. Photon absolute energy calibration

To estimate possible systematic effects due to miscalibration of the absolute photon energy, we examine how well the peak values in the kinematically-fitted distributions of $\rm E_\gamma^{low}$ for $\Upsilon(2S) \to \gamma\gamma\Upsilon(1S)$ candidates are calibrated with respect to those expected. The largest deviation is 0.2 MeV for the $J = 2$ peak position when an e^+e^- final state is selected. It is well reproduced in our MC samples with input masses of $\Upsilon(1S, 2S)$ as well as of $\chi_{bJ}(1P)$ based on the latest information [2]. These photon energies are kinematically-fitted variables, with $\rm E_\gamma^{low}$ and $\rm E_\gamma^{high}$ constrained to a fixed value for any given $\Upsilon(1S)$ momentum, so any shift in $\rm E_\gamma^{low}$ must be compensated by a corresponding one of opposite sign in $\rm E_\gamma^{high}$. Based on these observations, we conservatively vary signal positions by $\rm E_\gamma^{high}\pm 1$ MeV and simultaneously by $\rm E_\gamma^{low}\mp 1$ MeV.

4. Additional contributing uncertainties

Other possible systematic effects that we have investigated include a variation in the (small) branching fraction for the transition through $\chi_{b0}(1P)$ and insertion of an explicit fixed background component from $\Upsilon(3S) \to \pi^0\pi^0\Upsilon(1S)$.

D. Results on analysis of $\Upsilon(3S) \to \gamma\gamma\ell^+\ell^-$

Taking the above systematic uncertainties into account, we now arrive at the final results for the product of branching fractions for each of the transitions as shown in Table VIII. Also shown are comparisons to results from other analyses. The first uncertainty is the statistical uncertainty, the second is the overall systematic uncertainty, and the third (when applicable) is the uncertainty due to external inputs.

VI. RESULTS AND CONCLUSIONS

We obtain product branching fractions for the exclusive processes $\Upsilon(2S) \to \gamma\chi_{b0,1,2}(1P) \to \gamma\gamma\Upsilon(1S)$ (Table V) and $\Upsilon(3S) \to \gamma\chi_{b1,2}(1P) \to \gamma\gamma\Upsilon(1S)$ (Table VIII), where $\Upsilon(1S)$ is identified by its decay to e^+e^- and $\mu^+\mu^-$.

The extracted $\mathcal{B}[\chi_{bJ}(1P) \to \gamma\Upsilon(1S)]$ are the most precise to date for $J = 1,\ 2$, while for $J = 0$ this represents the first observation of this transition. These branching frac-

TABLE VII. Estimates of relative systematic uncertainties (in %) for this analysis, for each J, and the sum of $J = 1$ and 2. The first six entries are calculated for both spins. The fit to the sum of $J = 1$ and 2 has better stability against our binning scheme variations since yields of $J = 1$ and 2 are statistically anti-correlated, resulting in smaller variations in terms of their sum. For the rightmost column, the entry for "MC simulation" includes not only statistical errors of reconstruction efficiencies, but also the total uncertainties of the measured branching fractions on the weighted efficiency.

Contribution	$J = 2$	$J = 1$	$J = 1$ and 2
$N_{\Upsilon(3S)}$		1.7	
Track-finding		1.0	
Photon-finding		2.0	
Reduced χ^2 requirement		4.9	
Lepton identification		1.1	
Lepton flavor difference		1.2	
QED background	—	—	8.8
Include $\Upsilon(3S)\to\pi^0\pi^0\Upsilon(1S)$	0.3	1.2	0.5
$\chi_{b0}(1P)$ Yield variation	0.0	0.6	0.2
Binning scheme	3.3	11.6	2.7
Photon energy resolution	2.3	3.7	—
Photon absolute energy	9.1	11.0	—
MC simulation	—	—	0.7
Total	11.6	17.5	11.0

TABLE VIII. Final results of this analysis. Here, $\mathcal{B}1 = \mathcal{B}[\Upsilon(3S) \to \gamma\chi_{bJ}(1P)]$, $\mathcal{B}2 = \mathcal{B}[\chi_{bJ}(1P) \to \gamma\Upsilon(1S)]$, and $\mathcal{B}3 = \mathcal{B}[\Upsilon(1S) \to \ell^+\ell^-]$. We use $\mathcal{B}3 = (2.48 \pm 0.05)\%$ [2] and $\mathcal{B}2 = (18.5 \pm 0.5)\%$), $(33.0 \pm 0.6)\%$ from Sec. IV for $J = 2$ and $J = 1$, respectively, to extract $\mathcal{B}1 \times \mathcal{B}2$ as well as $\mathcal{B}1$. The first three rows show results from this work while the second three rows show previous results. Here, the first errors are statistical, the second errors are systematic, and the third errors (when applicable) are uncertainties due to external sources.

	$J = 1$	$J = 2$	$J = 1$ and 2
$\mathcal{B}1 \times \mathcal{B}2 \times \mathcal{B}3$ (10^{-5})	$1.33 \pm 0.30 \pm 0.23$	$3.56 \pm 0.40 \pm 0.41$	$4.96 \pm 0.37 \pm 0.55$
$\mathcal{B}1 \times \mathcal{B}2$ (10^{-4})	$5.38 \pm 1.20 \pm 0.94 \pm 0.11$	$14.35 \pm 1.62 \pm 1.66 \pm 0.29$	$19.99 \pm 1.50 \pm 2.20 \pm 0.40$
$\mathcal{B}1$ (10^{-3})	$1.63 \pm 0.36 \pm 0.28 \pm 0.09$	$7.74 \pm 0.88 \pm 0.88 \pm 0.38$	—
$\mathcal{B}1 \times \mathcal{B}2 \times \mathcal{B}3$ (10^{-5}) [6]	—	—	$5.20 \pm 0.54 \pm 0.52$
$\mathcal{B}1 \times \mathcal{B}2$ (10^{-4}) [19]	—	—	$12^{+4}_{-3} \pm 0.9$
$\mathcal{B}1$ (10^{-3}) [7]	< 1.9	< 20.3 $(11 \pm 6 \pm 2 \pm 1)$	—

TABLE IX. Comparison of measurements and theoretical predictions [4] for suppressed E1 transition rates $\Gamma[\Upsilon(3S) \to \gamma\chi_{bJ}(1P)]$ and ratios $\Gamma_{J=1}/\Gamma_{J=0} \equiv \Gamma[\Upsilon(3S) \to \gamma\chi_{b1}(1P)]/\Gamma[\Upsilon(3S) \to \gamma\chi_{b0}(1P)]$, $\Gamma_{J=2}/\Gamma_{J=0} \equiv \Gamma[\Upsilon(3S) \to \gamma\chi_{b2}(1P)]/\Gamma[\Upsilon(3S) \to \gamma\chi_{b0}(1P)]$, and $\Gamma_{J=2}/\Gamma_{J=1} \equiv \Gamma[\Upsilon(3S) \to \gamma\chi_{b2}(1P)]/\Gamma[\Upsilon(3S) \to \gamma\chi_{b1}(1P)]$. The CLEO III values are based on $\Gamma_{\rm total}[\Upsilon(3S)] = (20.32 \pm 1.85)$ keV [2] and are obtained by taking the central value of the measurement for the $J = 0$ state [9] and the values for $J = 1$ and 2 from this work. The last row shows $\Gamma_{J=1}/\Gamma_{J=0}$ and $\Gamma_{J=2}/\Gamma_{J=0}$ when scaling rates according to $E_\gamma^3 \times (2J + 1)$.

	$\Gamma_{J=0}$ (eV)	$\Gamma_{J=1}$ (eV)	$\Gamma_{J=1}/\Gamma_{J=0}$	$\Gamma_{J=2}$ (eV)	$\Gamma_{J=2}/\Gamma_{J=0}$	$\Gamma_{J=2}/\Gamma_{J=1}$
CLEO III (This expt.)	–	33 ± 10	0.54 ± 0.25	157 ± 30	2.58 ± 1.01	4.75 ± 1.75
Inclusive expt. [9]	61 ± 23	–		–		
$\chi_{bJ}(1P)$ exclusive expt. [7]	< 186	< 38		< 413		
Moxhay–Rosner (1983)	25	25	1.0	150	6.0	6.0
Gupta *et al.* (1984)	1.2	3.1	2.6	4.6	3.8	1.5
Grotch *et al.* (1984) (a)	114	3.4	0.03	194	1.7	57
Grotch *et al.* (1984) (b)	130	0.3	0.002	430	3.3	1433
Daghighian–Silverman (1987)	42	(c)	(c)	130	3.1	(c)
Fulcher (1990)	10	20	2.0	30	3.0	1.5
Lähde (2003)	150	110	0.7	40	0.3	0.4
Ebert *et al.* (2003)	27	67	2.5	97	3.6	1.4
$E_\gamma^3 \times (2J + 1)$			2.4		3.6	1.5

(a) Scalar confining potential. (b) Vector confining potential.
(c) The authors did not provide a prediction for $\Gamma[\Upsilon(3S) \to \gamma\chi_{b1}(1P)]$.

tions appear to be systematically smaller than the theoretical predictions (see Appendix A), indicating that the hadronic widths of $\chi_{bJ}(1P)$ might have been underestimated.

The extracted $\mathcal{B}[\Upsilon(3S) \to \gamma\chi_{b1,2}(1P)]$ may be compared with the branching fraction previously measured by CLEO, $\mathcal{B}[\Upsilon(3S) \to \gamma\chi_{b0}(1P)] = (0.30 \pm 0.04 \pm 0.10)\%$ [9], providing tests of relativistic corrections to electric dipole matrix elements. Table IX shows comparison against some theoretical predictions in terms of transition rates as well as ratios of transition rates while Fig. 6 shows the ratios pictorially. It might be worth revisiting these calculations in light of our new experimental results.

ACKNOWLEDGMENTS

We gratefully acknowledge the effort of the CESR staff in providing us with excellent luminosity and running conditions. D. Cronin-Hennessy thanks the A.P. Sloan Foundation. J. Rosner thanks Fermilab for hospitality during part of this investigation. This work was supported by the National Science Foundation, the U.S. Department of Energy, the Natural Sciences and Engineering Research Council of Canada, and the U.K. Science and Technology Facilities Council.

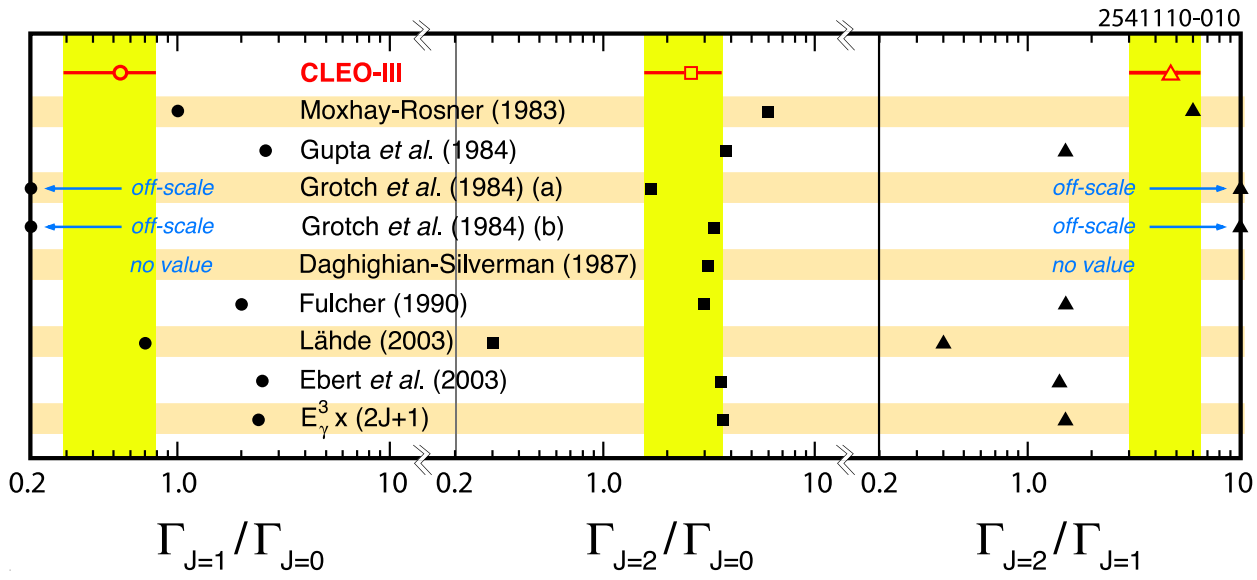

FIG. 6. Illustration of ratios of suppressed E1 transition rates, $\Gamma_{J=1}/\Gamma_{J=0}$ (circles), $\Gamma_{J=2}/\Gamma_{J=0}$ (squares), and $\Gamma_{J=2}/\Gamma_{J=1}$ (triangles) from Table IX.

Appendix A: Comparison of branching fractions $\mathcal{B}[\chi_{bJ}(1P) \to \gamma\Upsilon(1S)]$ with predictions

The measured branching fractions for $\chi_{bJ}(1P) \to \gamma\Upsilon(1S)$ may be compared with the predictions [4, 20] summarized in Table X. Most of the predicted branching fractions for these electric dipole transitions are systematically larger than the experimental values, indicating that the hadronic widths Γ_h were underestimated. A modest increase in the assumed value of $\alpha_S(m_b^2)$ leads to much better agreement with experiment. As one example, the values in Ref. [20] were calculated for $\alpha_S(m_b^2) = 0.18$. For this value it was found that $\Gamma_h[\chi_{b(0,1,2)}(1P)] = (791, 38.3, 132.3)$ keV, while the E1 transition rates were predicted to be $\Gamma[\chi_{b(0,1,2)}(1P) \to \gamma\Upsilon(1S)] = (26.1, 32.8, 37.8)$ keV. The hadronic widths scale for the $J = 0$ and $J = 2$ states $\alpha_S^2(m_b^2)$ times known QCD correction factors [21], while for the $J = 1$ state they scale as $\alpha_S^3(m_b^2)$. (The QCD correction factor for $J = 1$ is not known [21] and will be ignored.)

Using the scale factors, values of α_S, and the QCD correction factors described in the previous paragraph, we predict

$$\begin{aligned}
\frac{\Gamma_h[\chi_{b0}(1P)]}{791\text{ keV}} &= \left(\frac{\alpha_S(m_b^2)}{0.18}\right)^2 \frac{1 + 10.0\alpha_S(m_b^2)/\pi}{1.573}, \\
\frac{\Gamma_h[\chi_{b1}(1P)]}{38.3\text{ keV}} &= \left(\frac{\alpha_S(m_b^2)}{0.18}\right)^3, \text{ and} \\
\frac{\Gamma_h[\chi_{b2}(1P)]}{132.3\text{ keV}} &= \left(\frac{\alpha_S(m_b^2)}{0.18}\right)^2 \frac{1 - 0.1\alpha_S(m_b^2)/\pi}{0.994}.
\end{aligned} \tag{A1}$$

The minimum χ^2 of a fit to the values determined in this work is found to be 1.45 for 2 degrees of freedom The value of α_S that minimizes χ^2 and the corresponding error (defined by the range for which $\Delta\chi^2 \leq 1$ from the minimum) are $\alpha_S(m_b^2) = 0.214 \pm 0.006$. This is quite consistent with the determination of Ref. [22] for a scale of 5 GeV (see Fig. 5 there).

TABLE X. Comparison of our results for $\mathcal{B}[\chi_{bJ}(1P) \to \gamma\Upsilon(1S)]$ with some theoretical predictions [4, 20], in units of 10^{-2}.

Reference	$J = 0$	$J = 1$	$J = 2$
CLEO III	1.73 ± 0.35	33.0 ± 2.6	18.3 ± 1.4
Moxhay–Rosner (1983)	3.8	50.6	22.3
Gupta *et al.* (1984)	4.1	56.8	26.7
Grotch *et al.* (1984) (a)	3.1	41.9	19.4
Grotch *et al.* (1984) (b)	3.3	43.9	20.3
Daghighian–Silverman (1987)	2.3	31.6	16.6
Kwong–Rosner (1988)	3.2	46.1	22.2
Fulcher (1990)	3.1	39.9	18.6
Lähde (2003)	3.3	45.7	21.1
Ebert *et al.* (2003)	3.7	51.5	23.6

(a) Scalar confining potential. (b) Vector confining potential.

At this value, the rescaled values predicted in the approach of Ref. [20] are $\mathcal{B}[\chi_{b0,1,2}(1P) \to \gamma\Upsilon(1S)] = (2.1, 33.8, 16.8)\%$ and $\Gamma_{\rm tot}[\chi_{b0,1,2}(1P)] = (1221, 97, 225)$ keV.

The predicted ratio

$$R \equiv \frac{\Gamma_h(\chi_{b0}(1P))}{\Gamma_h(\chi_{b2}(1P))} = \frac{15}{4}\frac{1 + 10.0\alpha_S(m_b^2)/\pi}{1 - 0.1\alpha_S(m_b^2)/\pi} \tag{A2}$$

is roughly $R = 5.92 + 12[\alpha_S(m_b^2) - 0.18]$, to be compared with the value $R = 8.6 \pm 3.2$ based on the observed branching fractions. Thus, the QCD corrections go in the right direction to modify the uncorrected value of $15/4 = 3.75$.

[1] E. Eichten *et al.*, Rev. Mod. Phys. **80**, 1161 (2008).

[2] K. Nakamura *et al.* (Particle Data Group), J. Phys. G **37**, 075021 (2010).

[3] A. K. Grant, J. L. Rosner, A. Martin, J. M. Richard and J. Stubbe, Phys. Rev. D **53**, 2742 (1996) [arXiv:hep-ph/9506315].

[4] P. Moxhay and J. L. Rosner, Phys. Rev. D **28**, 1132 (1983); S. N. Gupta, S. F. Radford, and W. W. Repko, Phys. Rev. D **30**, 2424 (1984); H. Grotch, D. A. Owen, and K. J. Sebastian, Phys. Rev. D **30**, 1924 (1984); F. Daghighian and D. Silverman, Phys. Rev. D **36**, 3401 (1987); J. P. Fulcher, Phys. Rev. D **42**, 2337 (1990); T. A. Lähde, Nucl. Phys. A **714**, 183 (2003); D. Ebert, R. N. Faustov, and V. O. Galkin, Phys. Rev. D **67**, 014027 (2003).

[5] U. Heintz *et al.* (CUSB Collaboration), Phys. Rev. D **46**, 1928 (1992).

[6] T. Skwarnicki (CLEO Collaboration), in *Proceedings of the 31st International Conference on High Energy Physics (ICHEP 2002), Amsterdam, The Netherlands, 24-31 Jul 2002*, edited by S. Bentvelsen, P. de Jong, J. Koch, and E.Laenen [Nucl. Phys. B, Proc. Suppl. 117, 698 (2003)], available online by inputting the authors name (Skwarnicki) and the journal title (unabbreviated) at http://www.sciencedirect.com.

[7] D. M. Asner *et al.* (CLEO Collaboration), Phys. Rev. D **78**, 091103 (2008).
[8] Q. He *et al.* (CLEO Collaboration), Phys. Rev. Lett. **101**, 192001 (2008).
[9] M. Artuso *et al.* (CLEO Collaboration), Phys. Rev. Lett. **94**, 032001 (2005).
[10] Y. Kubota *et al.*, Nucl. Instrum. Meth. A **320**, 66 (1992).
[11] D. Peterson *et al.*, Nucl. Instrum. Meth. A **478**, 142 (2002).
[12] J. V. Bennett *et al.* (CLEO Collaboration), Phys. Rev. Lett. **101**, 151801 (2008); R. E. Mitchell *et al.* (CLEO Collaboration), Phys. Rev. Lett. **102**, 011801 (2009); P. U. E. Onyisi *et al.* (CLEO Collaboration), Phys. Rev. D **82**, 011103(R) (2010).
[13] D.J. Lange, Nucl. Instrum. Methods Phys. Res., Sect. A **462**, 152 (2001).
[14] S. R. Bhari *et al.* (CLEO Collaboration), Phys. Rev. D **79**, 011103 (2009).
[15] W. Walk *et al.* (Crystal Ball Collaboration), Phys. Rev. D **34**, 2611 (1986).
[16] F. Pauss *et al.* (CUSB Collaboration), Phys. Lett. B **130**, 439 (1983).
[17] C. Klopfenstein *et al.* (CUSB Collaboration), Phys. Rev. Lett. **51**, 160 (1983).
[18] C. M. Carloni Calame *et al.*, Nucl. Phys. Proc. Suppl. **131**, 48 (2004); C. M. Carloni Calame, Phys. Lett. B **520**, 16 (2001); C. M. Carloni Calame *et al.*, Nucl. Phys. B **584**, 459 (2000).
[19] U. Heintz *et al.* (CUSB Collaboration), Phys. Rev. D **46**, 1928 (1992).
[20] W. Kwong and J. L. Rosner, Phys. Rev. D **38**, 279 (1988).
[21] W. Kwong. P. Mackenzie, R. Rosenfeld, and J. L. Rosner, Phys. Rev. D **37**, 3210 (1988).
[22] S. Bethke, Eur. Phys. J. C **64**, 689 (2009) [arXiv:0908.1135 [hep-ph]].